Ion mobility studies of Pyrroloquinoline Quinone Aza-Crown Ether - Lanthanide Complexes

Alexander Schäfer,[b] Violeta A. Vetsova,[a] Erik K. Schneider,[b] Manfred Kappes[b,c], Michael Seitz[d], Lena J. Daumann[a]*, Patrick Weis[b]*

[a]*V. A. Vetsova, Prof. Dr. L. J. Daumann*

Department of Chemistry

Ludwig Maximilian University of Munich

Butenandtstraße 5–13, 81377 Munich (Germany)

**E-mail: lena.daumann@cup.lmu.de*

[b]*A. Schäfer, Dr. E. K. Schneider, Prof. Dr. M. Kappes, Dr. P. Weis*

Karlsruhe Institute of Technology

Institute of Physical Chemistry

Fritz-Haber-Weg 2, 76128 Karlsruhe (Germany)

**E-mail: patrick.weis@kit.edu*

[c] *Prof. Dr. M. Kappes*

Karlsruhe Institute of Technology

Institute of Nanotechnology

Hermann von Helmholtz Pl 1,76344 Eggenstein Leopoldshafen (Germany)

[d] *Prof. Dr. M. Seitz*

University of Tübingen

Institute of Inorganic Chemistry

Auf der Morgenstelle 18, 72076 Tübingen (Germany)

** Author to whom correspondence should be addressed*

Abstract:

Lanthanide-dependent enzymes and their biomimetic complexes have arisen as an interesting target of research in the last decade. These enzymes, specifically, pyrroloquinoline quinone (PQQ)-bearing methanol dehydrogenases, efficiently turn over alcohols to the respective aldehydes. To rationally design bioinspired alcohol dehydrogenation catalysts, it is imperative to understand the species involved in catalysis. However, given the extremely flexible coordination sphere of lanthanides, it is often difficult to assess the number and nature of the active species. Here we show how such questions can be addressed by using a combination of ion mobility spectrometry, mass spectrometry and quantum chemical calculations to study the test systems PQQ and lanthanide-PQQ-crown ether ligand complexes. Specifically, we determine the gas phase structures of $[PQQH_2]^-$, $[PQQH_2+H_2O]^-$, $[PQQH_2+MeOH]^-$, $[PQQ\text{-}15c5+H]^+$ and $[PQQ\text{-}15c5+Ln+NO_3]^+$ (Ln=La to Lu, except Pm). In the latter case a trend to smaller collision cross sections across the lanthanide series is clearly observable, in line with the well-known lanthanide contraction. We hope that in future such investigations will help to guide the design and understanding of lanthanide based biomimetic complexes optimized for catalytic function.

Introduction:

It was assumed for a long time that lanthanide(III) ions, in spite of their similarity to calcium(II) in size, acidity and coordination behaviour do not contribute to life on earth in the form of enzymes.[1] However, in 2007, in the volcanic mud pot of Solfatara, a bacterium (*Methylacidiphilum fumariolicum*, SolV) was discovered that could only be cultivated in the laboratory by addition of water from its original habitat.[2] Eventually it turned out that the high lanthanide concentrations (µM) in the mud pot water were responsible for the bacterial growth.[3] In the last decade it was shown that lanthanides play an important role in the active sites of methanol dehydrogenases (MDH), enzymes that catalyse the oxidation of methanol to formaldehyde in the context of the C1 metabolism in bacteria.[4,5,6,7,8,9,10] Despite the chemically very similar properties, the choice of lanthanide shows a sometimes considerable influence on the metabolism and thus on the growth of bacteria with the corresponding lanthanide-containing enzymes. Thus, it is mainly the early lanthanides that stimulate growth.[9] Besides the metal cation the active site of MDH contains a cofactor called pyrroloquinoline quinone (PQQ).[9] In addition to catalysing the conversion of methanol to formaldehyde, there is another interesting aspect of the PQQ chemistry. Lumpe et al. were recently able to show significant selectivity when precipitating lanthanide ions from aqueous solution by the addition of PQQ.[11] For this purpose, the resulting precipitate from a solution with lanthanum and another lanthanide (Ce-Lu) was analysed and depending on the element, La:Ln ratios between 4:6 (Ce) and 7:3 (Lu) were observed. Since it is already known that some aza-crown ethers also prefer the complexation of early lanthanides and that their complexes undergo a structural change in the series of lanthanides[12], the combination of PQQ and an aza-crown ether in a single molecule is the logical next step. The ligand PQQMe_2-1-aza-15-crown-5 (PQQ-15c5, see scheme 1) was first synthesized in 2000 by Itoh and Fukuzumi through coupling of a PQQ precursor with an aza-crown ether.[13] Recently, Vetsova et al. reported an improved synthesis route towards this ligand and investigated its lanthanide complexing properties as well as their ability to oxidize alcohols to aldehydes.[14] These studies comprised the combination of both condensed and gas phase methods, such as UV-vis, NMR and EPR spectroscopy as well as ion mobility mass spectrometry (IMMS) and collision induced dissociation (CID) studies. It turned out that the reaction yield depends not only on the metal center but also on the choice of counterion and base. Since in condensed phase the chemical environment is not as well defined as one might hope (various interconverting conformers, protomers, solvent adducts are often simultaneously present), gas phase studies offer the opportunity to probe the *intrinsic* molecular properties in a better controlled environment. The focus of this gas phase study is therefore on the structure of isolated PQQ and lanthanide-PQQ-15c5 complexes (for all lanthanoides except PM, while the preceding study[14] focused on La and Lu) with a well-defined number of solvent molecules and counterions. For this purpose, we use a combination of ion mobility spectrometry, mass spectrometry and quantum chemical calculations. This methodology has been applied by us and others to reveal the structures of molecular ions, complexes as well as reaction intermediates.[15,16,17] Note, that IMS based structure determination in gas phase (in contrast to NMR in condensed phase) is still a rapidly developing field which requires validation for new substance classes which have not yet been extensively addressed (such as lanthanide complexes). The fairly rigid structure of deprotonated $[PQQH_2]^-$ thus represents an ideal test system for the ion mobility method. In the following, we apply it to more flexible ions such as solvent- and counterion-adducts with and without lanthanides.

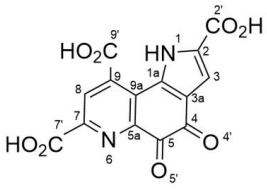

PQQH$_3$

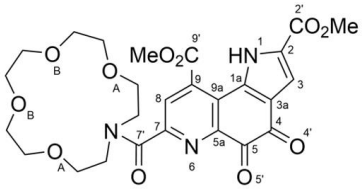

PQQ-15c5

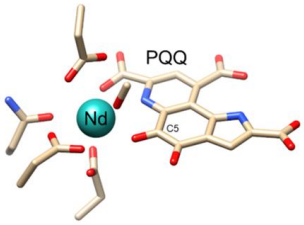

Scheme 1: Structures of neutral PQQ (PQQH$_3$) and PQQ-15c5. Active site of Nd-MDH isolated from *Methylacidimicrobium thermophilum* AP8 (PDB: 7O6Z). Shown are truncated coordinating amino acid residues, the cofactor PQQ and MeOH in the stick representation and neodymium as green sphere.[18]

Experimental Section:

Instrumental:

The ion mobility measurements were performed with a Bruker timsToF instrument. The operating principles of trapped ion mobility spectrometry (TIMS) are described elsewhere.[19] Briefly, an ion packet is pulse injected into an electrodynamical trap (the so called TIMS tunnel) filled with a flowing buffer gas (N_2). The resulting drift motion is compensated by a variable electrostatic field. The different types of ions contained in the packet are separated in space according to their mobility and eluted by ramping the field. In all experiments we operated the instrument at the highest feasible mobility resolution (ca. 150 -200) by using the slowest feasible ramp speeds (*via* narrow ion mobility windows and long ramp times of 500 ms). The TIMS tunnel is coupled with a quadrupole mass filter and a TOF-MS (resolution > 25000) that is operated with a high repetition rate (several kHz). The resulting 2D ion mobility-m/z data are deconvoluted into mobilograms with the instrument software (Data Analysis 5.0). For ion mobility and mass calibration we use Agilent TuneMix, a mixture for fluorinated phosphazenes, with the high precision mobility data of Stow *et al.* as reference.[20] Ion mobilities are translated into experimental collision cross sections ($^{TIMS}CCS_{N2}$) with the Mason-Schamp equation.[21] The $^{TIMS}CCS_{N2}$ in turn can be directly compared with theoretically modelled collision cross sections and thus enable structure determination in gas phase. The simultaneous occurrence of several isomers can be inferred, independent of any modelling, if bi- or multimodal mobilograms are observed or if peaks are significantly broader than the experimental resolution. Experiments were performed both in positive and negative mode (see below).

Theoretical modelling:

In order to identify the relevant isomers/conformers we performed density functional theory (DFT) calculations with the Turbomole package[21-22,23] using the TPSS functional[24-28] and def2-SVP[29-33] basis set.[34] For each species considered, we created a series of 10-20 meaningful starting geometries (differing in deprotonation site, conformation of the central PQQ-unit, relative orientation of counterion and solvent adduct). These geometries were constructed and preoptimized at force-field level with the Avogadro package[35] and used as xyz-coordinate input files for the DFT based geometry optimization. All geometries are fully optimized without any symmetry restrictions. Often, different starting geometries converge to the same final geometry. The Turbomole output comprises optimized xyz-geometries and relative energies. Since DFT calculations are known to give accurate geometries, but less reliable energies, we consider in the following at least all structures as reasonable candidates that are within 1 eV to the one found to be lowest in energy. Based on these candidate structures we

simulate theoretical collision cross sections. For this purpose, we perform trajectory method calculations to model the drift motion of the respective molecular ion in the buffer gas (N_2). For this the ion-buffer gas interaction is modelled by a Lennard-Jones potential plus ion-induced dipole and ion-quadrupole interaction with element specific LJ-parameters. The ion-induced dipole and ion-quadrupole interaction depend on the partial charge distribution of the drifting ion, we obtain these values by a Mulliken population analysis based on the DFT-calculation. With these input parameters, a large number (ca. 10^6) of ion-buffer gas trajectories is calculated, the thus obtained scattering angles are numerically integrated and finally a theoretical cross section $^{theo}CCS_{N2}$ is obtained. The closer theoretical and experimental cross sections and the lower the relative energy of the respective structure, the more likely it is the dominant species in the experimental mobilogram. All calculations were performed with the IMoS package (IMoS 1.09) with the standard LJ-parameters implemented.[36,37,38]

Sample preparation:

$PQQH_3$ was obtained *via* extraction from Dr's Best vitamin capsules as a disodium salt and obtained in its fully protonated form as described previously.[39] The PQQ-15c5 ligand was synthetized and purified as described elsewhere.[14] The lanthanide nitrates where obtained from Sigma Aldrich (Germany). The metal-ligand complex is formed by adding the respective Ln^{3+} salt to a solution of PQQ-15c5 (acetonitrile, 0.5 mmol/l, 1:1 ratio).

Results and discussion:

Upon electrospray ionization of a solution of $PQQH_3$ in DMSO (with 1%v/v H_2O and MeOH) we obtain in negative mode $[PQQH_2]^-$, $[PQQH_2+H_2O]^-$, and $[PQQH_2+MeOH]^-$. The corresponding mobilograms are shown in figure 1.

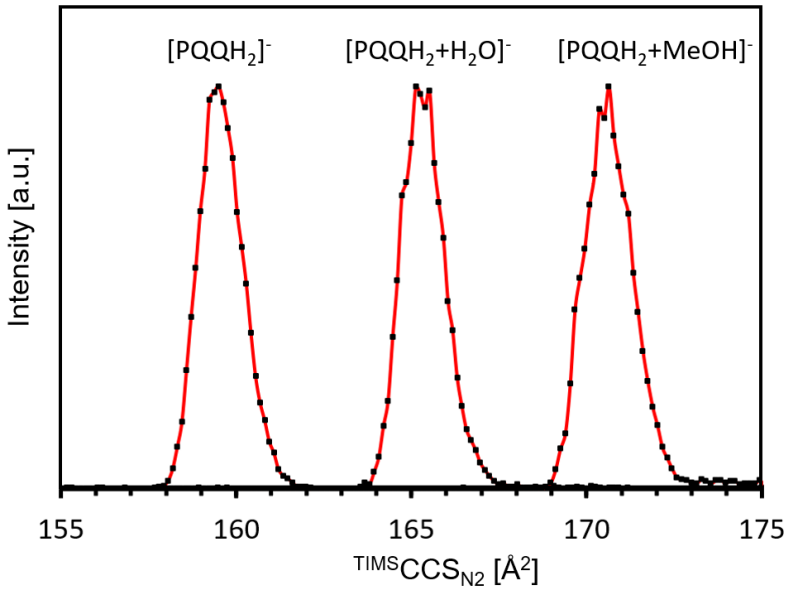

Figure 1: Typical mobilograms of $[PQQH_2]^-$, $[PQQH_2+H_2O]^-$ and $[PQQH_2+MeOH]^-$.

In all cases we observe one narrow peak with a peak width corresponding to the instrumental resolution of ca. 200. This can be interpreted in three ways: 1) Only one isomer ion is created upon ESI, or 2) Several isomers are present, but their CCS differ by less than 0.5 % (ca. 1 Å^2). 3) Several isomers with larger CCS differences are present, but they interconvert much faster than the timescale of the

experiment (100ms). To shed more light into this issue we calculated theoretical CCS ($^{theo}CCS_{N2}$) based on DFT optimized structures (see figure 2) and Mulliken charges. The results are summarized in table 1.

$[PQQH_2]^-$: The experimental $^{TIMS}CCS_{N2}$ is 159.5 ± 0.5 Å^2. In the lowest energy candidate structure that we obtain (structure 1a) N1 is deprotonated, all three carboxylic acid groups remain protonated, and there are two hydrogen bonds to N1 and N6 (for the numbering of the respective atoms see scheme 1). This structure has a $^{theo}CCS_{N2}$ of 161.3 Å^2 which is ca. 1% above the experimental value. Structure 1b is a conformer thereof with the hydrogen of the carboxylic group at C2 rotated (see figure 2, arrow). Both energy (+0.02 eV) and CCS (160.9 Å^2) are basically unchanged. Structure 1c is another conformer of 1a, the carboxylic group at C7 is rotated and therefore there is no hydrogen bond to N6 (see figure 2, arrow). This increases the energy by 0.35 eV, the $^{theo}CCS_{N2}$ is increases slightly to 162.4 Å^2. Based on CCS alone we cannot distinguish between these structures. Regarding structures 1a to 1c, it might be counterintuitive that N1 is deprotonated instead of the carboxylic acid function at C9 (note, that the latter is more acidic in condensed phase). This reflects the fact that in aqueous solution a COO^--function can be stabilized more efficiently by solvent molecules. This stabilization is missing in gas phase. In order to shed more light into this issue we performed some geometry-restricted DFT-calculations. We increased the O-H distance from its optimized value of 1.07 Å (with a corresponding N-H distance of 1.46 Å) up to 1.5 Å and optimized the remaining degrees of freedom. The corresponding N-H distance decreases to ca. 1.1 Å (consistent with a covalent bond) but the energy increases by ca. 0.14 eV (see figure S1). A similar discrepancy between the preferred protonation sites (O vs. N) in both liquid phase and gas phase is already known in the literature.[40] In structure 2 the C7 carboxylic group is deprotonated and N6 protonated. This structure is 0.55 eV higher in energy and has a cross section of 164.7 Å^2, i.e. ca. 3% above the experimental value. Again, there is an isoenergetic conformer with the C2-carboxylic group rotated, analogous to structure 1a vs 1b (not shown). For a C7 carboxylic group-H-N6 distance variation by a geometry-restricted DFT calculation see figure S2. Other structures are even higher in energy, such as structure 3, +0.93 eV (carboxylic acid group at C2 deprotonated) and have significantly larger CCS: 169.9 Å^2, ca. 7% above experiment. Therefore, such protomers can be ruled out based on relative energy and CCS. (Compare a similar combined IMS, cryo-IR, DFT study on biliverdin, where only conformers within 0.2 eV to the lowest are observed in experiment).[15] To summarize, with the combination of DFT based geometry optimization and trajectory calculations we can reproduce the experimental CCS for $[PQQH_2]^-$ within 1% if we take only the lowest energy structures calculated (1a and 1b) into account. This validates the method and the choice of input parameters (LJ-parameters, Mulliken charges, see above).

Table 1: Comparison of calculated and experimental CCS for $[PQQH_2]^-$.

	$^{TIMS}CCS_{N2}$ [Å^2]	Structure	$^{theo}CCS_{N2}$ [Å^2]	relative Energy [eV]
$[PQQH_2]^-$	159.5 ± 0.5	1a	161.3	0
		1b	160.9	0.02
		1c	162.4	0.35
		2	164.7	0.55
		3	169.9	0.93

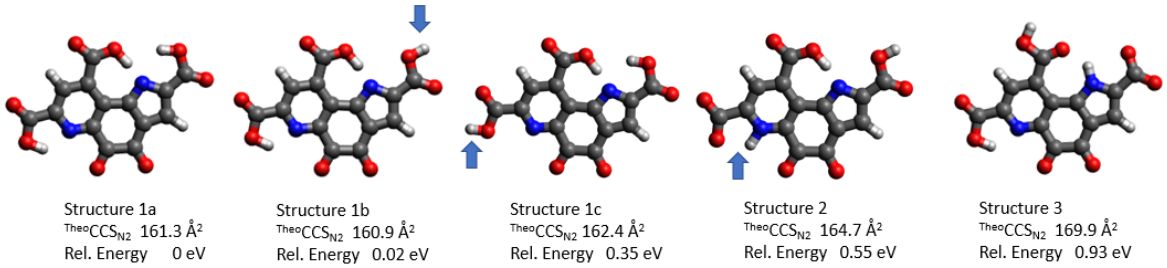

Figure 2: Calculated structures, relative energies and calculated collision cross sections for $[PQQH_2]^-$. The blue arrows highlight the differences between structures 1a, 1b, 1c and 2

$[PQQH_2+H_2O]^-$ and $[PQQH_2+MeOH]^-$: In a second step we investigated the formation of solvent/reactant adducts with $PQQH_3$ by adding small amounts of water and methanol (1% v/v) to the solution of $PQQH_3$ in DMSO, respectively. In both cases the adducts are formed in intensities sufficient to measure their CCS. On first sight this is surprising since the ions have to pass the desolvation region and transfer capillary heated to 300°C (the high temperature is necessary to remove the DMSO). The resulting $[PQQH_2+H_2O]^-$ anion has a $^{TIMS}CCS_{N2}$ of 164.7 Å^2. Compared with the 159.5 Å^2 for the bare $[PQQH_2]^-$ anion, this is an increase of only 3%, although the overall number of atoms in the ion increases by 10%, from 29 to 32. This implies a rather compact structure of the water adduct. From condensed phase NMR measurements it is known that the carbonyl group at C5 readily adds water to form a geminal diol.[39,41] The C4 group can also be attacked by nucleophiles as was shown by Itoh *et al.* [13] We performed DFT-optimizations for various protomers of both C5-dioles but also for non-covalently bound water adducts. The results are summarized in table 2 and figure 3. The lowest energy structure is a C5-diol (structure 1) with a cross section of 163.8 eV, slightly below the experimental value of 164.7 Å^2. A conformer thereof (structure 2, protonated carboxylic group at C7 rotated) has one hydrogen bond less, is therefore 0.36 eV higher in energy and has a $^{TIMS}CCS_{N2}$ of 165.6 Å^2, slightly above the experimental value. It is likely that the two conformers can interconvert by rotation around the C7-C7' single bond on the timescale of the CCS-measurement and we therefore measure a time average. A C4-diol, as proposed by Itoh *et al*. [13] (structure 3) has a very similar CCS (164.4 Å^2), but it is 0.27 eV above structure 1. Non-covalently bound water adducts (structures 4 and 5) come very close in energy to structure 1 (+0.06 eV and +0.14 eV). Taking their uncertainty into account, we cannot distinguish between covalently and non-covalently bound adducts on the basis of DFT-based energies alone. However, the $^{TIMS}CCS_{N2}$ of the non-covalently bound water adducts are significantly larger, 169.0 Å^2 and 169.1 Å^2, and therefore structures 4 and 5 can be ruled out.

Table 2: Comparison of calculated and experimental CCS for $[PQQH_2+H_2O]^-$.

	$^{TIMS}CCS_{N2}$ [Å^2]	Structure	$^{theo}CCS_{N2}$ [Å^2]	relative Energy [eV]
$[PQQH_2+H_2O]^-$	164.7 ± 0.5	1	163.8	0
		2	165.6	0.36
		3	164.4	0.27
		4	169.0	0.06
		5	169.1	0.14

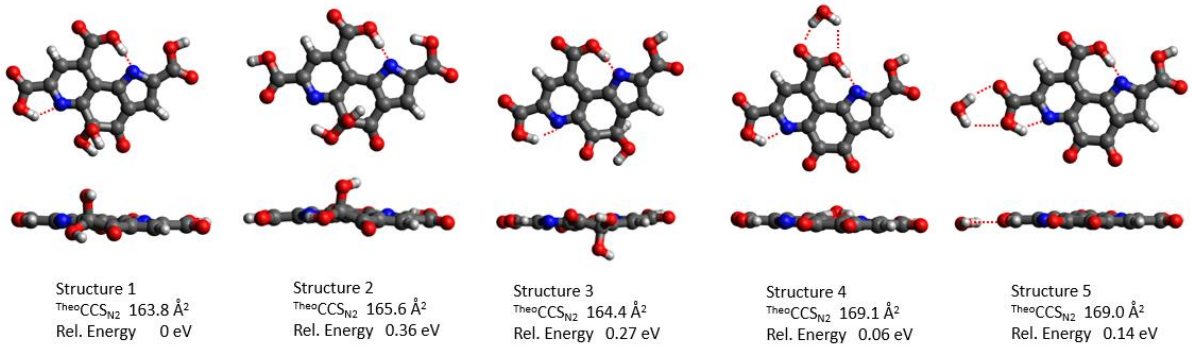

Figure 3: Calculated structures, relative energies and calculated collision cross sections for $[PQQH_2+H_2O]^-$.

For $[PQQH_2+MeOH]^-$ as well we obtain a single, narrow peak corresponding to an experimental CCS of 170.1 Å^2, see figure 1. As for the PQQ-water adducts, we take both covalently (at C5 and C4) and non-covalently bound structures into account in our DFT geometry optimizations. The results are summarized in table 3 and figure 4. Interestingly, in this case the non-covalently bound adduct with the methanol molecule associated with the C9' carbonyl group by a hydrogen bond (structure 4) turns out to be lowest in energy. Within 0.1 eV we find two other isomers: structure 5 (+0.05 eV), another non-covalently bound adduct (MeOH hydrogen bonded to O4') and structure 1 (+0.09 eV) with the methanol covalently bound to the carbonyl group at C5 as a hemiketal. A C4 hemiketal (structure 3) is significantly higher in energy by 0.25 eV. Structure 2 (+0.43 eV) is a conformer of structure 1 with one hydrogen bond less. Based on the ion mobility data we rule out the non-covalently bound isomers ($^{theo}CCS_{N2}$ = 175.7 Å^2 and 176.0 Å^2, respectively versus $^{TIMS}CCS_{N2}$ = 170.1 Å^2). On the other hand, we confirm the covalently bound structures, since their CCS agree within the experimental uncertainty with the measurement. Among these, structure 1 is clearly favoured based on energy and CCS.

Table 3: Comparison of calculated and experimental CCS for $[PQQH_2+MeOH]^-$.

	$^{TIMS}CCS_{N2}$ [Å^2]	Structure	$^{theo}CCS_{N2}$ [Å^2]	relative Energy [eV]
$[PQQH_2+MeOH]^-$	170.1 ± 0.5	1	169.9	0.09
		2	171.1	0.43
		3	171.8	0.25
		4	175.7	0
		5	176.0	0.05

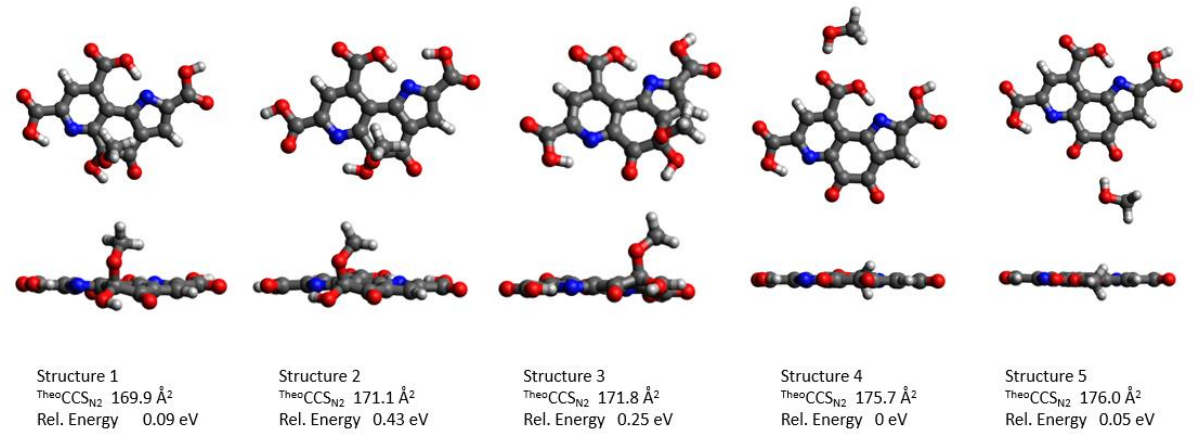

Figure 4: Calculated structures (top and side views), relative energies and calculated collision cross sections for $[PQQH_2+MeOH]^-$.

[PQQ-15c5+H]$^+$: The mobilogram of [PQQ-15c5+H]$^+$ consists of three distinct peaks, the largest centered at 225.2 Å^2 and two smaller peaks at 222.4 Å^2 and 228.2 Å^2, respectively, see figure 5 and table 4. This implies that there are at least three protomers/conformers that do not interconvert on the timescale of our ion mobility measurement, i.e. within ca. 0.5 s. We performed a series of geometry optimizations and found a total of 15 different structures within 1 eV. In the lowest energy structure (figure 6, structure 1) the extra proton is bound to the pyridine-nitrogen N6 and *via* a hydrogen bridge to O_A on the crown ether group (cf. scheme 1). The arrangement is such that the PQQ and crown ether units are slightly tilted. The $^{theo}CCS_{N2}$ of this structure is 229.0 Å^2, which is ca. 2% below the main peak in the mobilogram. Structure 2 is a variant thereof with a hydrogen bridge to O_B instead. Both relative energy (+0.1 eV) and CCS (228.8 Å^2) are similar to structure 1. We find several conformers (=local minima) in our geometry optimizations that differ by the relative orientations of the methyl ester groups. Their CCS are close to 229 Å^2. Somewhat higher in energy (+0.43 eV) we find a structure (3) with the extra proton between O_B and O5. As a consequence, this structure is rather flat and therefore has a somewhat larger CCS of 233.3 Å^2. This structure could be responsible for the third peak (at 228.2 Å^2) in the mobilogram, if we accept a deviation of ca. 2%. A more compact geometry (structure 4, 226.4 Å^2) is obtained by protonation at N6 and hydrogen bond to O_A. As a consequence, the crown ether is folded back to the PQQ-unit with an angle of ca. 60°, see figure 6. This structure can explain the first peak in the mobilogram if we accept a 2% deviation between experiment and calculation, as before. However, this structure is ca. 0.55 eV higher in energy. To summarize, due to the rather flexible crown ether function a series of non-interconverting structures with similar energy but different CCS is feasible and obviously realized in the experiment as can be seen by the trimodal mobilogram. The calculations can reproduce the main features. A temperature-dependent NMR experiment of PQQ-15c5 in acetonitrile supports the high flexibility of the aza-crown moiety (Figure S3).

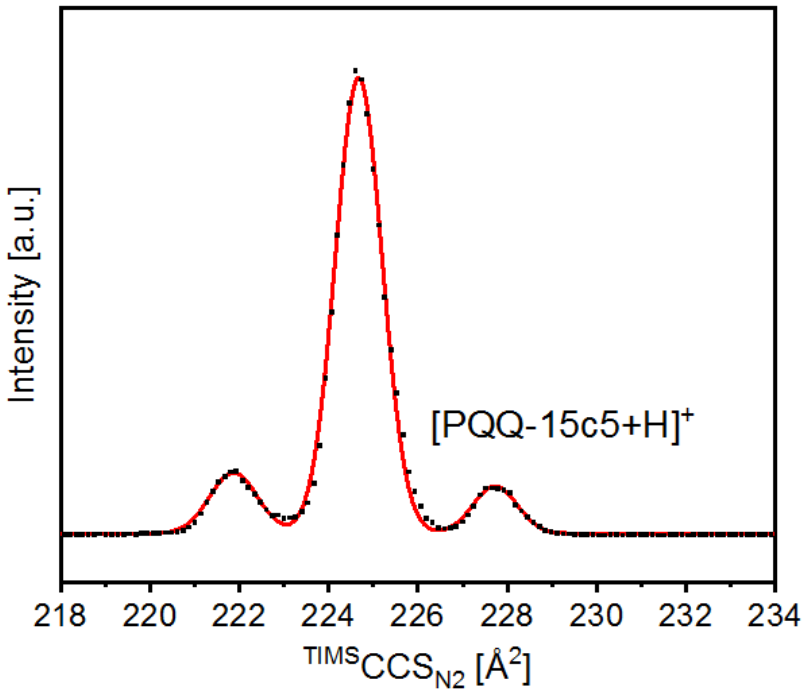

Figure 5: Typical mobilogram of [PQQ-15c5+H]$^+$.

Table 4: Comparison of calculated and experimental CCS for $[PQQ\text{-}15c5+H]^+$.

	$^{TIMS}CCS_{N2}$ [Å^2]	Structure	$^{theo}CCS_{N2}$ [Å^2]	relative Energy [eV]
$[PQQ\text{-}15c5+H]^+$	222.4 ± 0.5	1	229.0	0
	225.2 ± 0.5	2	228.8	0.1
		3	233.3	0.43
	228.2 ± 0.5	4	226.4	0.55

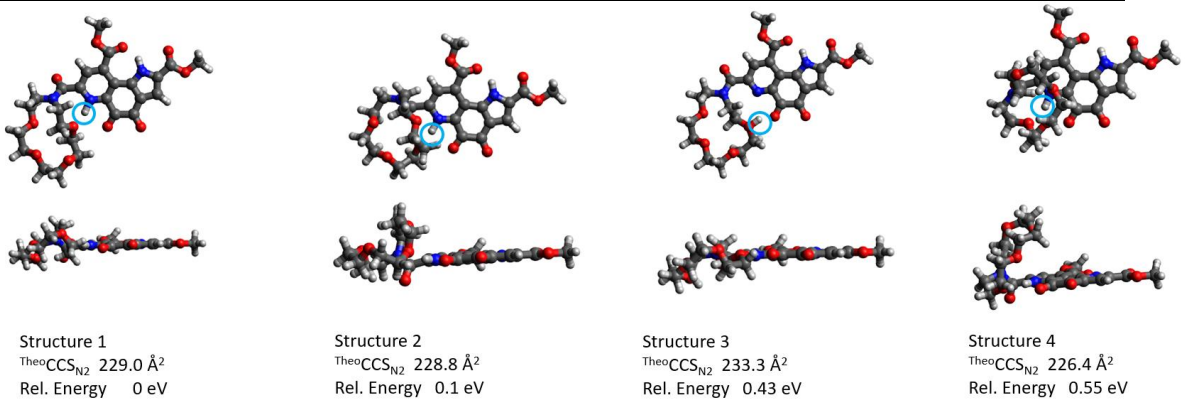

Figure 6: Calculated structures (top and side views), relative energies and calculated collision cross sections for $[PQQ\text{-}15c5+H]^+$. The blue circle indicates the protonation site.

$[PQQ\text{-}15c5+Ln+NO_3]^{2+}$: PQQ-15c5 easily forms metal complexes upon addition of M^{II} or M^{III} salts. With lanthanide(III) nitrates we observe upon electrospray ionisation the formation of complexes of the form $[PQQ\text{-}15c5+Ln+NO_3]^{2+}$. The nitrate counterion is strongly bound: upon collision induced dissociation no $NO_3^{0,-}$ or $NO_2^{0,-}$ loss is observed.[14] We see instead predominantly loss of MeOH, most likely from one of the ester functions in PQQ-15c5. Furthermore, we do not observe the complex ion without counterion, i.e. $[PQQ\text{-}15c5+Ln]^{3+}$. The mobilograms of all $[PQQ\text{-}15c5+Ln+NO_3]^{2+}$ complexes are rather simple with one narrow peak (figure 7). For La we obtain a $^{TIMS}CCS_{N2}$ of 281.8 ± 1.5 Å^2. There is a clear trend to smaller CCS when going from Ln to La, in line with the well-known lanthanide contraction. For Lu we obtain 278.7 ± 1.5 Å^2, see figure 8. Note that the 1.5 Å^2 uncertainty contains both calibration and statistical errors. Since we determine the CCS of all $[PQQ\text{-}15c5+Ln+NO_3]^{2+}$ ions (Ln=La to Lu – excepting Pm) under identical conditions, the relative uncertainties are well below 1 Å^2. We expect the lanthanide ion to interact with the electronegative oxygen and nitrogen atoms of the PQQ- or crown ether moiety, and nitrate counterions. To determine the dominating geometry, we performed DFT-based geometry optimizations with the formalism described above. The results are summarized in figure 9 with lanthanum as an example. The other lanthanides show very similar, isostructural geometries. In the lowest energy structure (structure 1, figure 8, 9 and table 5), Ln is 9-coordinate with PQQ-15c5 acting as a heptadentate ligand (five donors of the aza-crown ether, pyridine nitrogen N6, quinone-oxygen at C5) and a chelating nitrate binding in bidentate fashion. In order to get a more quantitative idea about the coordination geometry and the trends along the lanthanide series, the DFT-optimized structures of all lanthanide complexes were investigated with a continuous shape measure (CShM) approach[42,43,44] using the computer program SHAPE 2.1.[45] All 13 idealized reference geometries implemented in SHAPE 2.1 for coordination number 9 were taken into account and the corresponding numerical value S for the CShM was calculated.[46,47] S can theoretically range between 0 (perfect fit to the ideal reference geometry) and 100 (no geometric similarity). Smaller S indicates smaller average deviation from the reference geometry. Table S1 in the Supporting Information shows the CShM values S for the 7 reference geometries with the S smallest values. According to the analysis, the coordination geometries are relatively irregular and cannot be well described as being close to a particular ideal polyhedron. The smallest S (values for all lanthanides are

found for the capped square-antiprismatic (CSAPR-9: 4.79 > S > 2.81) and the muffin-shaped (MFF-9: 4.48 > S > 2.68) geometries.[46,47] In addition, the distances Ln-X (X=O, N) in the inner coordination spheres of the lanthanides decrease as expected by 6.5% and 9.1% for individual bond lengths. This manifestation of the lanthanide contraction is perfectly within the normal range of trends found in the crystal structures of isostructural lanthanide complex series[48, 49,50], which is a very good indicator of the quality of the DFT qualculations.

Structure 1 of $[PQQ\text{-}15c5+La]^{3+}$ has a $^{theo}CCS_{N2}$ of 282.7 Å^2 which is within 1 Å^2 (0.3%) of the experimental value of 281.8 Å^2. We performed similar geometry optimizations for all lanthanides. In each case this structural motif is far more stable than other isomers (by more than 0.5 eV) . Calculated and experimental CCS deviate by less than 1% (except for Sm, 1.2 % and Gd, 1.2%), see figure 8 and table 5.

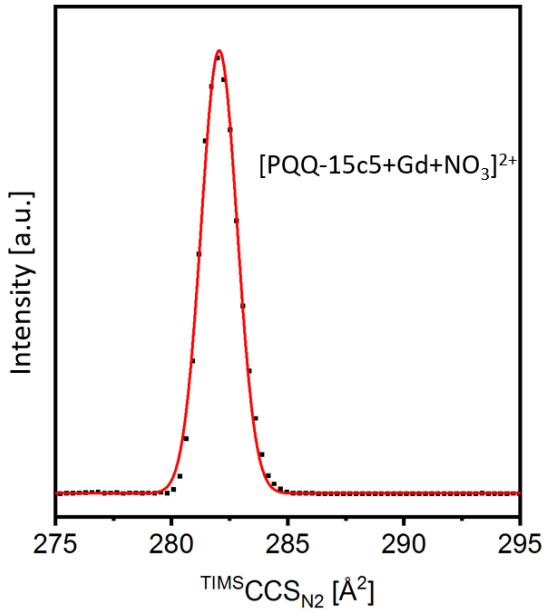

Figure 7: Typical mobilogram of $[PQQ\text{-}15c5+Ln+NO_3]^{2+}$, shown for Ln=Gd. Only one narrow peak is observable close to the instrumental resolution. Basically, the same mobilograms (one narrow peak) is obtained for all Ln = La to Lu.

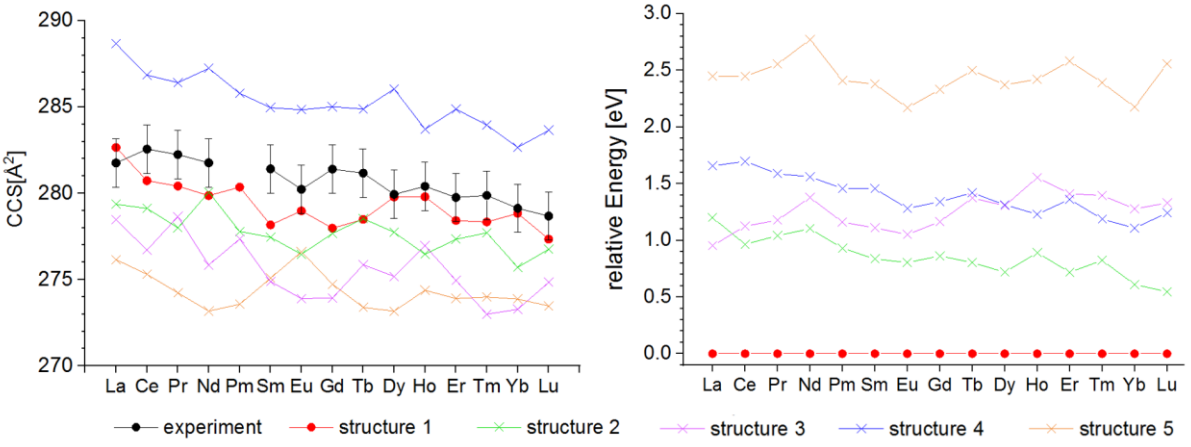

Figure 8, left: Experimental and calculated CCS of $[PQQ\text{-}15c5+Ln+NO_3]^{2+}$ for Ln=La to Lu. Black circles: Measurement. The error bars (±0.5%) comprise statistical and calibration errors. Since all measurements were performed at identical conditions (temperature, voltages across the TIMS-tunnel, ramp speed), we expect the relative errors to be even smaller, ca. 0.3%. The red circles correspond to the structure that has been found to be lowest in energy. The other symbols correspond to structures with higher energies. Right: relative energies of DFT optimized structures.

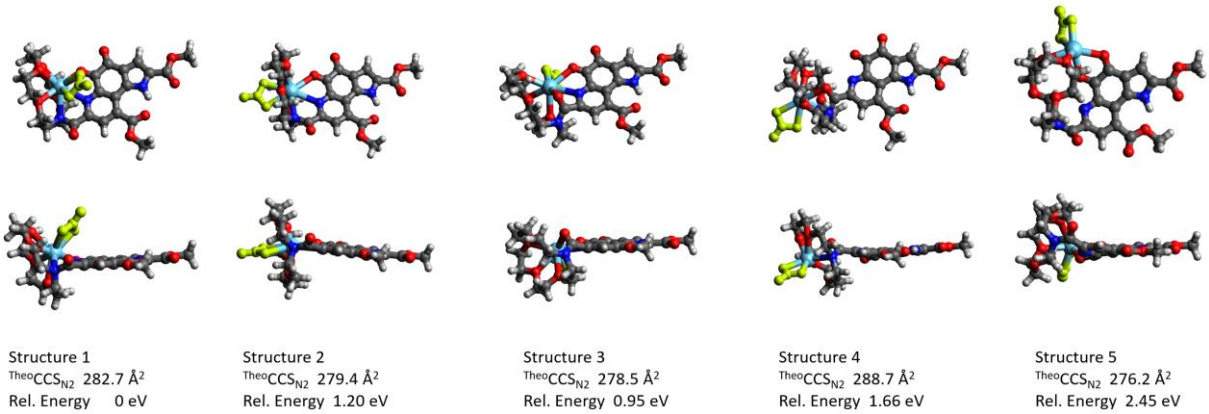

Figure 9: Calculated structures (top and side views), relative energies and calculated collision cross sections for $[PQQ\text{-}15c5+La+NO_3]^+$. The nitrate group is marked in yellow, lanthanide light blue.

Table 5: Comparison of calculated and experimental CCS for $[PQQ\text{-}15c5+Ln+NO_3]^{2+}$.

	exp CCS [Å²]	structure 1 CCS [Å²]	ΔE[eV]	structure 2 CCS [Å²]	ΔE[eV]	structure 3 CCS [Å²]	ΔE[eV]	structure 4 CCS [Å²]	ΔE[eV]	structure 5 CCS [Å²]	ΔE[eV]
La	281.8	282.7	0	279.4	1.20	278.5	0.95	288.7	1.66	276.2	2.45
Ce	282.6	280.7	0	279.1	0.96	276.7	1.13	286.9	1.70	275.3	2.45
Pr	282.2	280.4	0	278.0	1.04	278.6	1.18	286.4	1.59	274.2	2.55
Nd	281.8	279.9	0	280.1	1.10	275.8	1.38	287.2	1.56	273.2	2.77
Pm		280.4	0	277.8	0.93	277.4	1.16	285.8	1.46	273.6	2.41
Sm	281.4	278.2	0	277.5	0.84	274.9	1.11	285.0	1.46	275.1	2.38
Eu	280.2	279.0	0	276.5	0.80	273.9	1.05	284.8	1.28	276.6	2.17
Gd	281.4	278.0	0	277.7	0.86	273.9	1.16	285.0	1.34	274.7	2.33
Tb	281.2	278.5	0	278.5	0.80	275.9	1.37	284.9	1.42	273.4	2.50
Dy	279.9	279.8	0	277.7	0.72	275.2	1.30	286.0	1.31	273.2	2.37
Ho	280.4	279.8	0	276.5	0.89	277.0	1.55	283.7	1.23	274.4	2.42
Er	279.8	278.4	0	277.3	0.72	275.0	1.41	284.9	1.36	273.9	2.58
Tm	279.9	278.3	0	277.7	0.82	273.0	1.40	284.0	1.19	274.0	2.39
Yb	279.1	278.8	0	275.7	0.61	273.3	1.28	282.7	1.11	273.9	2.18
Lu	278.7	277.3	0	276.8	0.55	274.8	1.33	283.7	1.24	273.5	2.56

Besides this structure we found four other energy minima: Structures 2 and 3 are similar to structure 1, inasmuch as the metal atom is coordinated to the four crown ether oxygens as well as to N6 and the neighbouring quinone-oxygen, and the nitrate counterion, but in a different relative orientation, see figure 9. In structure 2 the nitrate and PQQ group are almost coplanar and on opposite sides of the metal atom, separated by the crown ether group. This structure is between 1.20 eV (La) and 0.55 eV (Lu) higher in energy than structure 1. Its calculated CCS deviates more (between 0.9 and 1.5%) from experiment than what we observe for structure 1. In structure 3 both nitrate and the PQQ unit cover one side of the metal center, and the crown ether the other side. Depending on the lanthanide, this structure is between 1.1 eV (Yb) and 1.7 eV (Ce) higher in energy than structure 1. Its cross section is on average ca. 2% below the experimental value. In structure 4 the metal center is not bound to N6 and the quinone-oxygen, i.e. it is here only complexed by the crown ether and the nitrate. This structure can be clearly ruled out: it is always more than 1.1 eV above structure 1, and its cross section on average ca. 2% above the experimental values (see table 5). We found a fifth structure with the metal center coordinated to both quinone-oxygens and only two of the oxygens of the crown ether. For all lanthanides it is more than 2 eV higher in energy, its cross section is more than 2% below the experiment can therefore be ruled out as well. To summarize, both on the basis of relative energy and cross section structure 1 is clearly favoured.

Conclusions

By a combination of ion mobility measurements and quantum chemical calculations we were able to identify the relevant gas phase structures of different PQQ derivatives and their complexes with solvent molecules, lanthanide(III) ions and nitrate counterions. To the best of our knowledge, this is the first ion mobility measurement across the complete series of complexes with lanthanide metal centers (except promethium). Even though there is only one lanthanide atom in the complexes comprising a total of 74 atoms, the trend to smaller CCS across the series is clearly observable (both experimentally and in the DFT-based geometry optimizations), in line with the well-known lanthanide contraction. PQQ is a notoriously difficult ligand to study, as it is reacts readily with a number of nucleophiles and shows complex speciation (including its different redox and protonation states) in solution. Here, we confirm the high reactivity of C5 towards nucleophiles (H_2O and MeOH) in the gas phase and assign structures that are in line with the reported solution models. In a second step, we investigated lanthanide complexes of a PQQ-inspired ligand that has previously been used as a biomimetic model for the alcohol oxidation in methanol dehydrogenases.[14] To evolve highly specific and well-defined lanthanide and quinone-based catalysts it is pivotal to understand different species, isomers and structures that may arise during catalysis. Here, we develop a benchmark for the study of such model systems and catalysts in the gas phase which can give hints into the function and optimal design of future biomimetic catalyst systems.

Supporting Information

Geometry restricted DFT calculations, temperature dependent NMR, CSM. All DFT-optimized structures are available as xyz-files in the supporting information

Acknowledgements

The Orbitrap@IPC/KIT used for this work was funded by DFG under INST 42/644-1 FUGG. MK thanks KIT for funding of the timsTOFMS. Development of experimental and theoretical IMS analysis methods used in this work was supported by the DFG funded CRC TRR 88 “3MET” (project C6). LJD thanks the DFG Project number 392552271 for funding.

References

[1] Lim, S.; Franklin, S. J., Lanthanide-binding peptides and the enzymes that Might Have Been. *Cell. Mol. Life Sci.* **2004**, *61*, 2184-2188.

[2] Pol, A.; Heijmans, K.; Harhangi, H. R.; Tedesco, D.; Jetten, M. S. M.; den Camp, H., Methanotrophy below pH1 by a new Verrucomicrobia species. *Nature* **2007**, *450*, 874-U17.

[3] Pol, A.; Barends, T. R. M.; Dietl, A.; Khadem, A. F.; Eygensteyn, J.; Jetten, M. S. M.; Op den Camp, H. J. M., Rare earth metals are essential for methanotrophic life in volcanic mudpots. *Environ. Microbiol.* **2014**, *16*, 255-264.

[4] Hibi, Y.; Asai, K.; Arafuka, H.; Hamajima, M.; Iwama, T.; Kawai, K., Molecular structure of La^{3+}-induced methanol dehydrogenase-like protein in Methylobacteriurn radiotolerans. *J. Biosci. Bioeng.* **2011**, *111*, 547-549.

[5] Fitriyanto, N. A.; Fushimi, M.; Matsunaga, M.; Pertiwiningrum, A.; Iwama, T.; Kawai, K., Molecular structure and gene analysis of Ce^{3+}-induced methanol dehydrogenase of Bradyrhizobium sp MAFF211645. *J. Biosci. Bioeng.* **2011**, *111*, 613-617.

[6] Nakagawa, T.; Mitsui, R.; Tani, A.; Sasa, K.; Tashiro, S.; Iwama, T.; Hayakawa, T.; Kawai, K., A Catalytic Role of XoxF1 as La^{3+}-Dependent Methanol Dehydrogenase in Methylobacterium extorquens Strain AM1. *PLoS One* **2012**, *7*, 7.

[7] Peplow, M., Unlocking the Lanthanome. *ACS Central Sci.* **2021**, *7*, 1776-1779.

[8] Skovran, E.; Martinez-Gomez, N. C., Just add lanthanides Some methanol-using bacteria may depend on lanthanide elements for carbon capture and energy generation. *Science* **2015**, *348*, 862-863.

[9] Daumann, L. J., Essential and Ubiquitous: The Emergence of Lanthanide Metallobiochemistry. *Angew. Chem.-Int. Edit.* **2019**, *58*, 12795-12802.

[10] Cotruvo, J. A., The Chemistry of Lanthanides in Biology: Recent Discoveries, Emerging Principles, and Technological Applications. *ACS Central Sci.* **2019**, *5*, 1496-1506.

[11] Lumpe, H., et al., The Earlier the Better: Structural Analysis and Separation of Lanthanides with Pyrroloquinoline Quinone. *Chem.-Eur. J.* **2020**, *26*, 10133-10139.

[12] Roca-Sabio, A.; Mato-Iglesias, M.; Esteban-Gomez, D.; Toth, E.; de Blas, A.; Platas-Iglesias, C.; Rodriguez-Blas, T., Macrocyclic Receptor Exhibiting Unprecedented Selectivity for Light Lanthanides. *J. Am. Chem. Soc.* **2009**, *131*, 3331-3341.

[13] Itoh, S.; Kawakami, H.; Fukuzumi, S., Development of the active site model for calcium-containing quinoprotein alcohol dehydrogenases. *J. Mol. Catal. B-Enzym.* **2000**, *8*, 85-94.

[14] Vetsova, V. A.; Fisher, K. R.; Lumpe, H.; Schäfer, A.; Schneider, E. K.; Weis, P.; Daumann, L. J., Pyrroloquinoline Quinone Aza-Crown Ether Complexes as Biomimetics for Lanthanide and Calcium Dependent Alcohol Dehydrogenases. *Chem.-Eur. J.* **2021**, *27*, 10087-10098.

[15] Zagorec-Marks, W.; Dodson, L. G.; Weis, P.; Schneider, E. K.; Kappes, M. M.; Weber, J. M., Structure and Cryogenic Ion Spectroscopy of Deprotonated Biliverdin. *J. Am. Chem. Soc.* **2021**, *143*, 17778-17785.

[16] Haler, J. R. N.; Lemaur, V.; Far, J.; Kune, C.; Gerbaux, P.; Cornil, J.; De Pauw, E., Sodium Coordination and Protonation of Poly(ethoxy phosphate) Chains in the Gas Phase Probed by Ion Mobility-Mass Spectrometry. *J. Am. Soc. Mass Spectrom.* **2020**, *31*, 633-641.

[17] Greisch, J. F., et al., Detection of Intermediates in Dual Gold Catalysis Using High-Resolution Ion Mobility Mass Spectrometry. *Organometallics* **2018**, *37*, 1493-1500.

[18] Schmitz, R. A.; Picone, N.; Singer, H.; Dietl, A.; Seifert, K. A.; Pol, A.; Jetten, M. S. M.; Barends, T. R. M.; Daumann, L. J.; Op den Camp, H. J. M., Neodymium as Metal Cofactor for Biological Methanol Oxidation: Structure and Kinetics of an XoxF1-Type Methanol Dehydrogenase. *mBio* **2021**, *12*, 14.

[19] Michelmann, K.; Silveira, J. A.; Ridgeway, M. E.; Park, M. A., Fundamentals of Trapped Ion Mobility Spectrometry. *J. Am. Soc. Mass Spectrom.* **2015**, *26*, 14-24.

[20] Stow, S. M., et al., An Interlaboratory Evaluation of Drift Tube Ion Mobility-Mass Spectrometry Collision Cross Section Measurements. *Anal. Chem.* **2017**, *89*, 9048-9055.

[21] Revercomb, H. E.; Mason, E. A., Theory of Plasma Chromatography/ Gaseous Electrophoresis - A Review. *Anal. Chem.* **1975**, *47*, 970-983.

[22] Furche, F.; Ahlrichs, R.; Hättig, C.; Klopper, W.; Sierka, M.; Weigend, F., Turbomole. *Wiley Interdiscip. Rev.-Comput. Mol. Sci.* **2014**, *4*, 91-100.

[23] Turbomole V7.5.1 2021, a Development of University of Karlsruhe and Forschungszentrum Karlsruhe GmbH, 1989-2007, Turbomole GmbH, since 2007; Available from https://www.turbomole.org.

[24] Dirac, P. A. M., The quantum theory of the electron. *Proceedings of the Royal Society of London. Series A, Containing Papers of a Mathematical and Physical Character* **1928**, *117*, 610-624.

[25] Perdew, J. P.; Wang, Y., Accurate and simple analytic representation of the electron-gas correlation energy. *Physical review B* **1992**, *45*, 13244.

[26] Perdew, J. P.; Wang, Y., Erratum: Accurate and simple analytic representation of the electron-gas correlation energy [Phys. Rev. B 45, 13244 (1992)]. *Physical Review B* **2018**, *98*, 079904.

[27] Slater, J. C., A simplification of the Hartree-Fock method. *Physical review* **1951**, *81*, 385.

[28] Tao, J.; Perdew, J. P.; Staroverov, V. N.; Scuseria, G. E., Climbing the density functional ladder: Nonempirical meta–generalized gradient approximation designed for molecules and solids. *Physical Review Letters* **2003**, *91*, 146401.

[29] Eichkorn, K.; Treutler, O.; Öhm, H.; Häser, M.; Ahlrichs, R., Auxiliary basis sets to approximate Coulomb potentials. *Chemical physics letters* **1995**, *240*, 283-290.

[30] Schäfer, A.; Horn, H.; Ahlrichs, R., Fully optimized contracted Gaussian basis sets for atoms Li to Kr. *The Journal of Chemical Physics* **1992**, *97*, 2571-2577.

[31] Weigend, F., Accurate Coulomb-fitting basis sets for H to Rn. *Physical chemistry chemical physics* **2006**, *8*, 1057-1065.

[32] Weigend, F.; Ahlrichs, R., Balanced basis sets of split valence, triple zeta valence and quadruple zeta valence quality for H to Rn: Design and assessment of accuracy. *Physical Chemistry Chemical Physics* **2005**, *7*, 3297-3305.

[33] Weigend, F.; Häser, M.; Patzelt, H.; Ahlrichs, R., RI-MP2: optimized auxiliary basis sets and demonstration of efficiency. *Chemical physics letters* **1998**, *294*, 143-152.

[34] Schäfer, A.; Horn, H.; Ahlrichs, R., Fully optimized contracted Gaussian basis sets for atoms Li to Kr. *J. Chem. Phys.* **1992**, *97*, 2571-2577.

[35] Hanwell, M. D.; Curtis, D. E.; Lonie, D. C.; Vandermeersch, T.; Zurek, E.; Hutchison, G. R., Avogadro: an advanced semantic chemical editor, visualization, and analysis platform. *Journal of Cheminformatics* **2012**, *4*, 17.

[36] Larriba, C.; Hogan, C. J., Free molecular collision cross section calculation methods for nanoparticles and complex ions with energy accommodation. *J. Comput. Phys.* **2013**, *251*, 344-363.

[37] Larriba, C.; Hogan, C. J., Ion Mobilities in Diatomic Gases: Measurement versus Prediction with Non-Specular Scattering Models. *J. Phys. Chem. A* **2013**, *117*, 3887-3901.

[38] Wu, T. Y.; Derrick, J.; Nahin, M.; Chen, X.; Larriba-Andaluz, C., Optimization of long range potential interaction parameters in ion mobility spectrometry. *J. Chem. Phys.* **2018**, *148*, 074102.

[39] Lumpe, H.; Daumann, L. J., Studies of Redox Cofactor Pyrroloquinoline Quinone and Its Interaction with Lanthanides(III) and Calcium(II). *Inorg. Chem.* **2019**, *58*, 8432-8441.

[40] Warnke, S.; Seo, J.; Boschmans, J.; Sobott, F.; Scrivens, J. H.; Bleiholder, C.; Bowers, M. T.; Gewinner, S.; Schöllkopf, W.; Pagel, K., Protomers of benzocaine: solvent and permittivity dependence. *Journal of the American Chemical Society* **2015**, *137*, 4236-4242.

[41] Zheng, Y. J.; Bruice, T. C., Conformation of coenzyme pyrroloquinoline quinone and role of Ca^{2+} in the catalytic mechanism of quinoprotein methanol dehydrogenase. *Proc. Natl. Acad. Sci. U. S. A.* **1997**, *94*, 11881-11886.

[42] Pinsky, M.; Avnir, D., Continuous symmetry measures. 5. The classical polyhedra. *Inorg. Chem.* **1998**, *37*, 5575-5582.

[43] Alvarez, S.; Alemany, P.; Casanova, D.; Cirera, J.; Llunell, M.; Avnir, D., Shape maps and polyhedral interconversion paths in transition metal chemistry. *Coord. Chem. Rev.* **2005**, *249*, 1693-1708.

[44] Alvarez, S.; Avnir, D.; Llunell, M.; Pinsky, M., Continuous symmetry maps and shape classification. The case of six-coordinated metal compounds. *New J. Chem.* **2002**, *26*, 996-1009.

[45] Llunell, M.; Casanova, D.; Cirera, J.; Alemany, P.; Alvarez, S., SHAPE 2.1; Universitat de Barcelona: Barcelona, Spain, 2013.

[46] Ruiz-Martinez, A.; Casanova, D.; Alvarez, S., Polyhedral structures with an odd number of vertices: Nine-coordinate metal compounds. *Chem.-Eur. J.* **2008**, *14*, 1291-1303.

[47] Ruiz-Martinez, A.; Casanova, D.; Alvarez, S., Polyhedral structures with an odd number of vertices: nine-atom clusters and supramolecular architectures. *Dalton Trans.* **2008**, 2583-2591.

[48] Seitz, M.; Oliver, A. G.; Raymond, K. N., The lanthanide contraction revisited. *J. Am. Chem. Soc.* **2007**, *129*, 11153-11160.

[49] Quadrelli, E. A., Lanthanide contraction over the 4f series follows a quadratic decay. *Inorg. Chem.* **2002**, *41*, 167-169.

[50] Shannon, R. D., Revised Effective Ionic-radii and Systematic Studies of Interatomic Distances in Halides and Chalcogenides. *Acta Crystallogr. Sect. A* **1976**, *32*, 751-767.